JOURNAL OF Materials CHEMISTRY

$Eu_5In_2Sb_6$, $Eu_5In_{2-x}Zn_xSb_6$: rare earth zintl phases with narrow band gaps

Seon-Mi Park,[a] Eun Sang Choi,[b] Woun Kang[b] and Sung-Jin Kim*[a]

[a]*Department of Chemistry, Ewha Womans University, #120-750 , Seoul, Korea. E-mail: sjkim@ewha.ac.kr; Fax: 82-2-3277-2384; Tel: 82-2-3277-2350*
[b]*Department of Physics, Ewha Womans University, #120-750 , Seoul, Korea*

Received 27th July 2001, Accepted 1st February 2002
First published as an Advance Article on the web 11th April 2002

The new Zintl phase $Eu_5In_2Sb_6$ was obtained from a direct element combination reaction in a sealed graphite tube at 870 °C and its structure was determined. It crystallizes in the orthorhombic space group *Pbam*(No. 55), with a unit cell of $a = 12.510(3)$ Å, $b = 14.584(3)$ Å, $c = 4.6243(9)$ Å, and $Z = 2$. $Eu_5In_2Sb_6$ shows the $Ca_5Ga_2As_6$–type structure and has a one-dimensional structure with infinite anionic double chains $[In_2Sb_6]^{10-}$ separated by Eu^{2+} ions. Each single chain is made of corner sharing $InSb_4$ tetrahedra. Two such tetrahedral chains are bridged by a Sb_2 group to form double chains. The compound satisfies the classical Zintl concept and is a narrow band gap semiconductor. The substitution of Zn for In atoms in $Eu_5In_2Sb_6$ resulted in an increase in hole concentration and the material is more metallic. Polycrystalline ingots of $Eu_5In_2Sb_6$ and $Eu_5In_{2-x}Zn_xSb_6$ showed electrical conductivity of $\sim$36 S cm^{-1}, $\sim$146 S cm^{-1} and Seebeck coefficient of $\sim$76 μV K^{-1}and $\sim$51 μV K^{-1} at room temperature, respectively.

Introduction

The structures of Zintl phases display a diversity of clusters, chains, nets, rings, and other polyanionic frameworks.[1,2] In Zintl phases, the electropositive atoms provide electrons to electronegative atoms in order to achieve an octet in the valence electron shell. Consequently, Zintl phases would be expected to be electron precise and to show semiconducting behavior. This electron transfer results in the formation of various complicated covalent anionic frameworks, stabilized by weakly bound electropositive cations. The great majority of Zintl phases are reported to be air- and moisture sensitive because of the highly electropositive alkali and alkaline earth element, such as Na, Ca, and Sr. Recently in attempts to develop thermoelectric materials, new air-stable heavy element analogues of the Zintl phases such as Ba_6Ge_{24},[1a] $Ba_4In_8Sb_{16}$,[1b] $Yb_5In_2Sb_6$,[2c] and $BaGa_2Sb_2$,[2k] were synthesized. All these compounds are composed of heavier cations and have narrow band-gaps, which is important for the thermoelectric properties. Among these compounds, $Yb_5In_2Sb_6$[2c] is the first example of a rare earth analogue of $Ca_5Al_2Bi_6$.

Here we describe another new rare earth analogue of the $A_5M_2Pn_6$ (A = Ca, Sr, Ba; M = Al, Ga, In; Pn = As, Sb, Bi) family, $Eu_5In_2Sb_6$, which is isoelectronic with $Yb_5In_2Sb_6$ but not isostructural. The band structures of the two rare earth phases are compared. We also synthesized $Eu_5In_{1.5}Zn_{0.5}Sb_6$ and its transport properties are compared with those of $Eu_5In_2Sb_6$.

Experimental section

Synthesis

The crystal used in the structure determination resulted from the reaction of a mixture of Eu (0.22 g, 1.45 mmol), In (0.07 g, 0.58 mmol) and Sb (0.21 g, 1.74 mmol) in a molar ratio of 5 : 2 : 6. The reaction mixtures were placed in a graphite tube and then sealed in an evacuated silica tube. The sealed mixtures were heated slowly up to 870 °C, kept at that temperature for 1 day, and subsequently cooled to room temperature over 1 day. From the reaction product, a few silvery plated crystals were obtained, along with a black powder. The X-ray powder diffraction pattern of the black powder sample agreed with the powder pattern calculated from single crystal data, indicating that the black powder was pure $Eu_5In_2Sb_6$. $Eu_5In_{2-x}Zn_xSb_6$($x = 0.5$) was obtained from reactions of a mixture of Eu (0.44 g, 2.90 mmol), In (0.1 g, 0.87 mmol), Zn (0.02 g, 0.29 mmol) and Sb (0.42 g, 3.48 mmol) in a molar ratio of 5 : 1.5 : 0.5 : 6. The reaction conditions were the same as for $Eu_5In_2Sb_6$. The X-ray powder pattern of $Eu_5In_{2-x}Zn_xSb_6$($x = 0.5$) also agreed with that of $Eu_5In_2Sb_6$ except for the relative peak intensities, and this indicates that the In atoms are substituted by Zn atoms without structural change. The compositions of $Eu_5In_2Sb_6$ and $Eu_5In_{2-x}Zn_xSb_6$ were confirmed by Energy-dispersive X-ray(EDX) analysis

Charge-transport measurements

DC electrical conductivity measurements were carried out by the low frequency AC lock-in technique using the conventional four probe technique. The applied current was about 20 μA with a frequency of 77 Hz. A pressed pellet of powder sample was ground to a bar shape with dimensions of 1.7 × 1.0 × 1.0 mm^3. 25 μm gold wires were attached to the sample using silver paste. Silver paste for current contacts covered the sample ends to improve current homogeneity. For thermoelectric power measurement, samples used in the conductivity measurements were mounted between two copper blocks which were heated by sinusoidal currents with the same frequency ($f_0 \sim 30$ mHz), but with 90 degree phase difference. The corresponding potential drop and temperature gradient with $2f_0$ frequency were measured by nanovoltmeters. The temperature gradients were measured using chromel-constantan thermocouples. Occasionally, the magnitudes of the thermoelectric power at room temperature were checked by the conventional DC slope technique. The thermoelectric power measurements techniques are detailed elsewhere.[3]

Table 1 Selected data from the single-crystal structure refinement of $Eu_5In_2Sb_6$

Empirical formula	$Eu_5In_2Sb_6$
Formula weight	1719.94
Temperature/K	293(2)
Wavelength (λ = Mo-Kα, Å)	0.71073
Crystal system	Orthorhombic
Space group	*Pbam* (No. 55)
Unit cell dimensions/Å	a = 12.510(3)
	b = 14.584(3)
	c = 4.6243(9)
Volume/Å^3	843.7(3)
Z	2
Density, ρ_{calc}/g cm^{-3}	6.770
Absorption coefficient/mm^{-1}	30.338
Reflections collected/unique	881
Data/restrains/parameters	845/0/42
Final R indices [$F_o^2 > 2\sigma(Fo^2)$][a]	R_1 = 0.0349, wR_2 = 0.1348
R indices ($F_o^2 > 0$)	R_1 = 0.0490, wR_2 = 0.1470
Largest DIFF. Peak and hole/e Å^{-3}	2.094 and −2.667

[a] $R_1 = [\Sigma||F_o|-|F_c||/\Sigma|F_o|$. $wR_2 = \{[\Sigma w(|F_o|-|F_c|)^2/[\Sigma w(F_o^2)^2]]\}^{1/2}$. $w = \sigma_F^{-2}$.

Electronic structure calculations

Electronic structure calculations were performed using the Hückel method within the framework of tight-binding approximation.[4] The program CAESAR for IBM-compatible PCs was used.[5] Density of state (DOS) and crystal orbital overlap populations (COOP) were calculated based on 216 K point sets of primitive orthorhombic structure.

Crystallographic studies†

A silver plated crystal was mounted on a glass fiber. X-Ray intensity data were collected at room temperature on a Enraf-Nonius CAD-4 single-crystal diffractometer with graphite monochromated Mo-Kα radiation (λ = 0.71073°). The unit cell parameters and the orientation matrix for data collection were obtained from the least-squares refinement, using the setting angles of 25 reflections in the range of 15.5° < 2θ(Mo-Kα) < 27.56°. Intensity data were collected over a 1/8 sphere of reciprocal space up to 49.92° in 2θ with the ω-2θ scan technique. The intensities of three standard reflections, measured every two hundred reflections, showed no significant deviations during the data collection. Empirical ψ-scan absorption correction was applied based on entire data sets. The observed Laue symmetry and systematic extinctions were indicative of the space group *Pbam*. The initial positions for all atoms were obtained from the direct methods. The structure was refined by full matrix least squares techniques with the use of the SHELXL-97 program.[6] The complete data collection parameters and details of structure solution and refinement results are given in Table 1. Final atomic positions are given in Table 2. Selected bond distances and angles are listed in Table 3.

Results and discussion

Structure

The structure of $Eu_5In_2Sb_6$ is an anisotropic one-dimensional structure and isotypic with $Ca_5Ga_2As_6$. The overall structure of this compound, viewed down the c-axis, is shown in Fig. 1(a). It is composed of infinite $[In_2Sb_6]^{10-}$ double chains separated by Eu^{2+} ions. The double chains stacked along the c-axis consist of two $InSb_4$ tetrahedral single chains bridged by Sb_2 dumbbell groups. Neighboring infinite double chains are crystallographically equivalent and related by b-glide and a-glide symmetry operations perpendicular to the a and b directions, respectively. The Eu^{2+} atoms are positioned between the double chains providing charge balance. There are three crystallographically unique Eu atoms, surrounded by Sb atoms of the double chains (Fig. 2). The geometry around the Eu atoms in $Eu_5In_2Sb_6$ is similar to that of Yb atoms in $Yb_5In_2Sb_6$. Eu(1) is coordinated to two In atoms at 3.676° and stabilized in seven fold coordination with Sb atoms in a capped trigonal prismatic geometry. Eu(2) and Eu(3) atoms are in distorted octahedral geometries with Sb atoms. Eu(3) has a different coordination environment from Yb atoms in $Yb_5In_2Sb_6$: Yb(3) in $Yb_5In_2Sb_6$ is surrounded by four Sb(3) atoms, but Eu(3) is surrounded by two Sb(3) atoms.

The $Ca_5Ga_2As_6$-type[7] (Fig. 1 (a)) and $Ca_5Al_2Bi_6$-type[8] (Fig. 1 (b)) have a structural difference in the packing pattern of double chains. Although Ca and Yb atoms have similar cationic radii and form compounds with the same anionic chain, they are stabilized in different structure types (Table 4). It is difficult to rationalize the difference in structure types by using only the size effect of the cations. Fig. 3 shows a side view of the double chain $_\infty^1[In_2Sb_6]^{10-}$ showing three crystallographically different Sb atoms and bond type labelings. The bond lengths in similar compounds are listed for a comparison in Table 4. As the cation radius in $Ca_5Ga_2As_6$-type compounds increases, the distances of In–Sb bonds (a, b, c in Fig. 3) also increase to fulfill the space requirement. But Sb(3)–Sb(3) distances do not show any clear feature depending on cation sizes. Even though cationic sizes are almost the same in $Ca_5In_2Sb_6$ and $Yb_5In_2Sb_6$, the Sb(3)–Sb(3) distance in $Ca_5In_2Sb_6$ is significantly shorter than that of $Yb_5In_2Sb_6$. The origin of the Sb(3)–Sb(3) bond difference in the two

Table 2 Atomic coordinates ($\times 10^4$) and equivalent isotropic displacement parameters (Å^2 $\times$ 10^3) for $Eu_5In_2Sb_6$

Atom	x	y	z	U(eq)[a]
Eu(1)	3275(1)	189(1)	0	14(1)
Eu(2)	0	0	0	12(1)
Eu(3)	9128(1)	7505(1)	0	13(1)
Sb(1)	1653(1)	8268(1)	0	13(1)
Sb(2)	1528(1)	940(1)	5000	11(1)
Sb(3)	5258(1)	956(1)	5000	12(1)
In(1)	3299(1)	2148(1)	5000	13(1)

[a] U(eq) is defined as one-third of the trace of the orthogonalized U_{ij} tensor.

Table 3 Selected distances/Å and angles/° in $Eu_5In_2Sb_6$[a]

Sb(1)–In(1) × 2	2.8304(16)	In(1)–Sb(1)–In(1)	109.55(9)
Sb(2)–In(1)	2.830(3)	In(1)–Sb(3)–Sb(3)	112.33(10)
Sb(3)–In(1)	3.006(3)	Sb(1)–In(1)–Sb(1)	109.55(9)
Sb(3)– Sb(3)	2.861(4)	Sb(1)–In(1)--Sb(2)	112.06(6)
Eu(1)–In(1) × 2	3.676(2)	Sb(1)–In(1)–Sb(3)	108.44(6)
Eu(1)–Sb(1)	3.461(2)	Sb(2)–In(1)–Sb(3)	106.11(9)
Eu(1)–Sb(2) × 2	3.3641(16)		
Eu(1)–Sb(3) × 2	3.3915(16)	Sb(1)–Eu(1)–Sb(3)#2	85.33(5)
Eu(1)–Sb(3) × 2	3.5708(18)	Sb(1)–Eu(1)–Sb(3)#1	131.38(4)
Eu(2)–Sb(1) ×2	3.2647(18)	Sb(1)–Eu(1)–Sb(1)#1	129.38(4)
Eu(2)–Sb(2) × 4	3.2991(13)	Sb(1)–Eu(1)–Sb(2)#1	83.27(5)
Eu(3)–Sb(1)	3.348(2)	Sb(1)#5–Eu(2)–Sb(1)	180.0
Eu(3)–Sb(1)	3.295(2)	Sb(2)#6–Eu(2)–Sb(1)	92.60(4)
Eu(3)–Sb(3) × 2	3.3228(16)	Sb(2)#6-Eu(2)-Sb(2)#1	180.0
Eu(3)–Sb(2) × 2	3.3410(17)	Sb(1)#7–Eu(3)–Sb(1)	179.41(5)
Eu(1)–Eu(2)	4.1063(16)	Sb(1)#7–Eu(3)–Sb(2)#5	90.05(5)
Eu(2)–Eu(3) × 2	3.7987(15)	Sb(1)#7–Eu(3)–Sb(3)#8	89.12(5)
Eu(1)–Eu(1)	4 .351(3)	Sb(2)#5–Eu(3)–Sb(3)#8	179.12(5)
Eu(1)–Eu(3)	4.072(2)		

[a] Symmetry transformations used to generate equivalent atoms: #1 (x, y, z + 1) #2 (−x + 1, −y, −z) #5 (−x, −y, −z) #6 (−x, −y, −z − 1) #7 (x − 0.5, −y − 0.5, z) #8 (−x + 0.5, y − 0.5, −z − 1).

†CCDC reference number 175836. See http://www.rsc.org/suppdata/jm/b1/b106812a/ for crystallographic files in .cif or other electronic format.

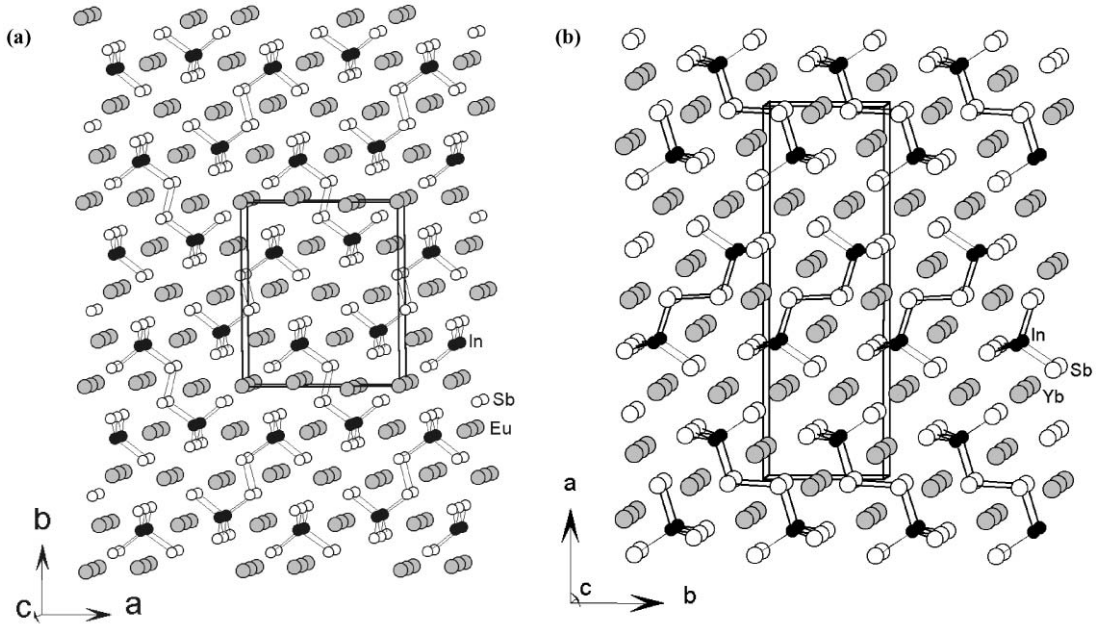

Fig. 1 (a) View down the *c* axis of the structure of $Eu_5In_2Sb_6$, (b) View down the *c* axis of the structure of $Yb_5In_2Sb_6$ with the orthorhombic unit cell outlined.

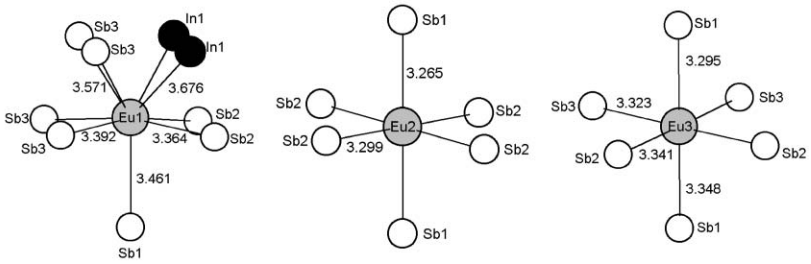

Fig. 2 Coordination of the Eu atoms in $Eu_5In_2Sb_6$ with Eu–In and Eu–Sb bond lengths/Å.

Table 4 Bond distances/Å in $Ca_5Ga_2As_6$ and $Ca_5Al_2Bi_6$-type phases

Compounds	a[a]	b[a]	c[a]	d[a]	Structure type
$Ca_5In_2Sb_6$	2.810	2.826	2.954	2.863	$Ca_5Ga_2As_6$
$Eu_5In_2Sb_6$	2.830	2.830	3.006	2.861	$Ca_5Ga_2As_6$
$Sr_5In_2Sb_6$	2.840	2.836	3.025	2.855	$Ca_5Ga_2As_6$
$Ba_5In_2Sb_6$	2.892	2.853	3.100	2.855	$Ca_5Ga_2As_6$
$Ca_5Al_2Bi_6$	2.806	2.803	2.860	3.184	$Ca_5Al_2Bi_6$
$Yb_5In_2Sb_6$	2.818	2.850	2.934	2.944	$Ca_5Al_2Bi_6$

[a]See bond types for a, b, c, and d in Fig. 3.

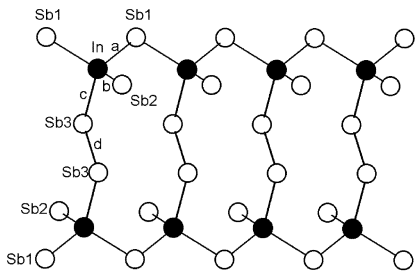

Fig. 3 A fragment of a infinite chain $[In_2Sb_6]^{10-}$ with atomic and bond labeling.

compounds is due to the σ* antibonding orbital of the Sb–Sb bond, therefore, a higher degree of electron transfer from Yb^{2+} to Sb(3)–Sb(3) antibonding is expected. The fact that there are a higher number of chemical bonds between Sb(3) and Yb atoms in $Yb_5In_2Sb_6$ than between Sb(3) and Eu atoms in $Eu_5In_2Sb_6$ supports the higher degree of antibonding character in Sb(3)–Sb(3), thus longer bond length in $Yb_5In_2Sb_6$.

Electronic structure

To understand the chemical bonding and physical properties of this material, band structure calculations were performed on the anionic frameworks $[In_2Sb_6]^{10-}$ of $Eu_5In_2Sb_6$ and $Yb_5In_2Sb_6$, and the results compared.[2c] The band structures were calculated by the extended Hückel formalism with atomic orbital parameters given in Table 5. Fig. 4 shows the total DOS for the $[In_2Sb_6]_n^{10n-}$ unit of $Eu_5In_2Sb_6$ and $Yb_5In_2Sb_6$. The overall features of the valence band in both $Eu_5In_2Sb_6$ and $Yb_5In_2Sb_6$ were similar except for the slightly narrower band width of valence and conduction bands of $Eu_5In_2Sb_6$. In the DOS plot for the $[In_2Sb_6]_n^{10n-}$ unit of $Eu_5In_2Sb_6$, the valence bands near the Fermi level arise primarily from p-orbitals of In atoms and p-orbitals of Sb atoms forming sp^3 hybridization mixed with corresponding s-orbitals. The peaks

Table 5 Atomic orbital parameters[a] used in extended Hückel calculations

Atom	Orbital	H_{ii}/eV[b]	$\xi 1$[c]	C1
In	5s	−18.8000	2.32300	1.00000
	5p	−11.7000	1.99900	1.00000
Sb	5s	−12.6000	1.90300	1.00000
	5p	−6.19000	1.67700	1.00000

[a]See Ref.10 [b]$H_{ii} = <\chi_i|H_{\text{eff}}|\chi_i>$, $i = 1,2,3,\cdots$.The value approximated by valence–state ionization potential. [c]Single-zeta STO's.

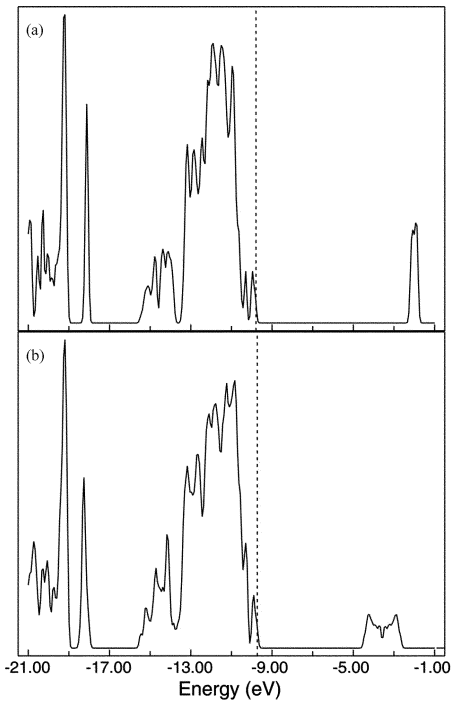

Fig. 4 Total DOS curve (a) $[In_2Sb_6]^{10-}$ of $Eu_5In_2Sb_6$ (b) $[In_2Sb_6]^{10-}$ of $Yb_5In_2Sb_6$[2c]. The Fermi levels are indicated by a vertical dashed line.

just below the Fermi level are mainly from p_z orbitals of Sb(3) with nonbonding character. The bottom of the conduction band mainly consists of p_y states of Sb(3). When rare earth cations were included in the calculation, the bandgaps of the two compounds were decreased by significant mixing interactions between the cation and anionic frameworks.[2c] $Ca_5Al_2Bi_6$-type compounds, $Yb_5In_2Sb_6$, and $Ca_5Al_2Bi_6$, have narrower bandgaps than $Ca_5Ga_2As_6$-type compounds, $Ca_5In_2Sb_6$, $Sr_5In_2Sb_6$, $Ba_5In_2Sb_6$, and $Eu_5In_2Sb_6$, which suggests that there is different covalency in the two types of compounds. Fig. 5 shows COOP plot projections of In–Sb and Sb–Sb

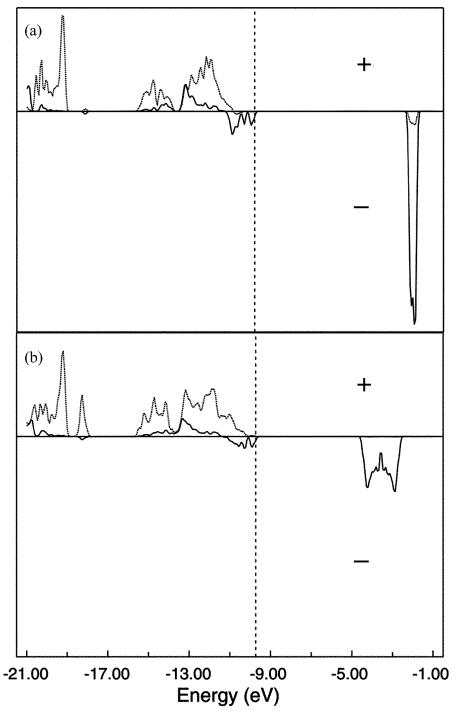

Fig. 5 COOP curves of In–Sb(dotted line) and Sb–Sb(solid line) bond. (a) COOP curve for $[In_2Sb_6]^{10-}$ of $Eu_5In_2Sb_6$ (b) COOP curve for $[In_2Sb_6]^{10-}$ of $Yb_5In_2Sb_6$.

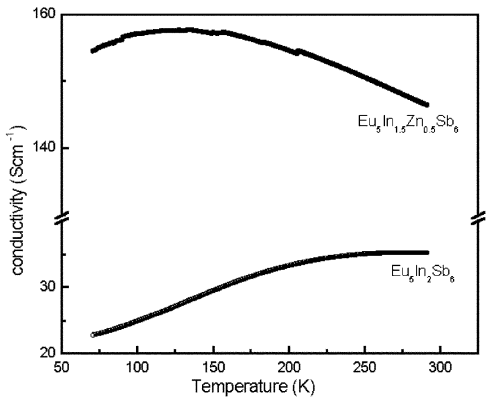

Fig. 6 Temperature dependence of the electrical conductivity for polycrystalline ingots of $Eu_5In_2Sb_6$ and $Eu_5In_{1.5}Zn_{0.5}Sb_6$.

bonds. In the projection of the In–Sb bond, all the valence states below E_f are from In–Sb bonding interactions consistent with maximized In–Sb bonding character. However, some of the Sb–Sb antibonding states just below the Fermi level are also filled suggesting a slight weakening of the bonding interaction in the Sb–Sb zigzag chains. Comparing band structures of $Yb_5In_2Sb_6$ and $Eu_5In_2Sb_6$, the slightly broader band width of valence states of $Yb_5In_2Sb_6$ seems to be related to the shorter bond length of In–Sb(3) and longer bond length of Sb(3)–Sb(3). The cumulated overlap populations of In–Sb in $Yb_5In_2Sb_6$ and $Eu_5In_2Sb_6$ are 0.61, 0.63 and Sb–Sb in $Yb_5In_2Sb_6$ and $Eu_5In_2Sb_6$ are 0.54, 0.56, which imply full single bonds.

Charge-transport measurements

Fig. 6 and Fig. 7 show the temperature dependence of electric conductivity and the Seebeck coefficient of $Eu_5In_2Sb_6$ and $Eu_5In_{1.5}Zn_{0.5}Sb_6$. The positive sign of the Seebeck coefficient indicates that the major carriers are holes for both $Eu_5In_2Sb_6$ and $Eu_5In_{1.5}Zn_{0.5}Sb_6$. Electric conductivity of polycrystalline ingots of $Eu_5In_2Sb_6$ was $\sim$36 S cm^{-1} and the Seebeck coefficient was $\sim$76 μV K^{-1} at room temperature. To increase electric conductivity by increasing hole concentration, we tried to substitute In atoms by Zn atoms. The result showed that the conductivity of $Eu_5In_{1.5}Zn_{0.5}Sb_6$ was increased to $\sim$146 S cm^{-1} and the Seebeck coefficient was $\sim$51 μV K^{-1} at room temperature.

We can speculate on the effect of Zn substitution on $Eu_5In_2Sb_6$ from the experimental results. First, we focus on the electrical conductivity data. The magnitude of conductivity increases about 4 times at room temperature by Zn substitution and the temperature dependence also shows a difference after Zn substitution. Although both samples show weak

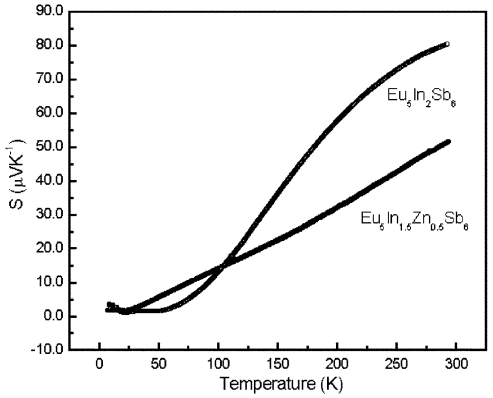

Fig. 7 Temperature dependence of the thermoelectric power for polycrystalline ingots of $Eu_5In_2Sb_6$ and $Eu_5In_{1.5}Zn_{0.5}Sb_6$.

temperature dependence in the measured temperature range, the temperature coefficient of resistance (TCR) is apparently different between them. TCR is positive for $Eu_5In_2Sb_6$ and negative for $Eu_5In_{1.5}Zn_{0.5}Sb_6$, which indicates metallic transport dominates for $Eu_5In_{1.5}Zn_{0.5}Sb_6$ while non-metallic for $Eu_5In_2Sb_6$.

The Seebeck coefficient decreases with cooling for both samples. For $Eu_5In_{1.5}Zn_{0.5}Sb_6$, the temperature dependence is more or less linear with a smaller room temperature value than that of $Eu_5In_2Sb_6$. $Eu_5In_2Sb_6$ shows some deviations from the linear temperature dependence. From the large magnitude of the Seebeck coefficient, which is higher than for ordinary metals by an order of magnitude, we assume that both semiconducting and metallic carriers are involved in the Seebeck coefficient. When two types of carriers are involved, the Seebeck coefficient will be expressed as[9]

$$\alpha_{total} = \frac{\sigma_1\alpha_1 + \sigma_2\alpha_2}{\sigma_1 + \sigma_2}$$

where $\sigma_1(\sigma_2)$ and $\alpha_1(\alpha_2)$ are the conductivity and the Seebeck coefficient of type 1(2) carriers respectively. If 1 denotes a metallic carrier and 2 denotes a semiconducting carrier, the low temperature Seebeck coefficient will be dominated by the metallic carrier since σ_1 is very high at low temperature and σ_2 goes to zero exponentially. Considering the shallow minimum near 50 K for $Eu_5In_2Sb_6$, we conjecture a contribution of negative metallic carriers for the Seebeck coefficient. By Zn substitution, the Seebeck coefficient decreases and the temperature dependence becomes more metallic.

Both the Seebeck coefficient and the conductivity measurements results indicate that Zn substitution makes the system more metallic. By Zn substitution, the density of carriers (holes in this case) increases, and the distance between the Fermi energy and the valence band edge decreases. Considering the positive TCR and the linear temperature dependence of the Seebeck coefficient for $Eu_5In_{1.5}Zn_{0.5}Sb_6$, we assume the 25% substitution of In by Zn almost closes the bandgap of the semiconducting band.

In summary, we have synthesized the rare earth Zintl compound $Eu_5In_2Sb_6$ with a narrow bandgap. From the electric conductivity and the Seebeck coefficient measurements, both metallic and semiconducting carriers seem to be involved in charge transport of this system. The substitution of Zn leads the system to be more metallic, which is evidenced by the increase of electric conductivity and the decrease of the Seebeck coefficients after substitution. The thermoelectric materials are evaluated by the figure of merit, Z, which is defined as $Z = S^2\sigma/\kappa$, where S is the Seebeck coefficient, σ is the electric conductivity, and κ is the thermal conductivity. The substitution of Zn may also enhance the Z value, however, overall thermoelectric capability can be improved by finding optimum concentrations of dopant and appropriate choice of dopants.

Acknowledgement

This work was supported by Korea Research Foundation Grant (KRF-2001-042-D00054).

References

1 (*a*) S.-J. Kim, S. Hu, C. Uher, T. Hogan, B. Huang, J. D. Corbett and M. G. Kanatzidis, *J. Solid State Chem.*, 2000, **153**, 321; (*b*) S.-J. Kim, S. Hu, C. Uher and M. G. Kanatzidis, *Chem. Mater.*, 1999, **11**, 3154.

2 (*a*) R. Lam and A. Mar, *Inorg. Chem.*, 1996, **35**, 6959; (*b*) R. Lam, J. Zhang and A. Mar, *J. Solid State Chem.*, 2000, **150**, 371; (*c*) S.-J. Kim, J. Ireland, C. R. Kannewurf and M. G. Kanatzidis, *J. Solid State Chem.*, 2000, **155**, 55; (*d*) S. Bobev and S. C. Sevov, *Inorg. Chem.*, 2000, **39**, 5930; (*e*) J. T. Vaughey and J. D. Corbett, *J. Am. Chem. Soc.*, 1996, **118**, 12098; (*f*) S. Kaskel and J. D. Corbett, *Inorg. Chem.*, 2000, **39**, 778; (*g*) S. Bobev and S. C. Sevov, *Inorg. Chem.*, 1999, **38**, 2672; (*h*) Z. Xu and A. M. Guloy, *J. Am. Chem. Soc.*, 1998, **120**, 7349; (*i*) M. J. Ferguson, R. E. Ellenwood and A. Mar, *Inorg. Chem.*, 1999, **38**, 4503; (*j*) E. Todorov and S. C. Sevov, *Angew. Chem., Int. Ed. Engl.*, 1999, **38**, 1775; (*k*) S.-J. Kim and M. G. Kanatzidis, *Inorg. Chem.*, 2001, **40**, 3781.

3 E. S. Choi, J. S. Brooks and J. S. Qualls, *Rev. Sci. Inst.*, 2001, **72**, 2392.

4 (*a*) R. Hoffman, *J. Chem. Phys.*, 1963, **39**, 1397; (*b*) E. Canadell and M.-H. Whangbo, *Chem. Rev.*, 1991, **91**, 965.

5 J. Ren, W. Liang and M.-H. Whangbo, CAESAR 1.0, PrimeColor Software, Inc., North Carolina State University.

6 G. M. Sheldrick, SHELXL-97, Program for Crystal Structure Refinement, University of Göttingen, Göttingen, Germany 1997.

7 (*a*) G. Cordier, H. Schäfer and M. Stelter, *Z. Naturforsch. B: Anorg. Chem. Org. Chem.*, 1985, **40**, 5; (*b*) G. Cordier and M. Stelter, *Z. Naturforsch. B: Chem. Sci.*, 1988, **43**, 463; (*c*) P. Verdier, P. L'Haridon, M. Maunaye and Y. Laurent, *Acta Crystallogr., Sect. B Struct. Crystallogr. Cryst. Chem.*, 1976, **32**, 726.

8 (*a*) G. Cordier, H. Schäfer and M. Stelter, *Z. Naturforsch. B: Anorg. Chem. Org. Chem.*, 1984, **39**, 727; (*b*) G. Cordier, H. Schäfer and M. Stelter, *Z. Naturforsch. B: Anorg. Chem. Org. Chem.*, 1985, **40**, 1100.

9 D. K. C. McDonald, *Thermoelectricity*, John Wiley & Sons, New York, 1962.

10 M. Wolfgang and L. Helmholz, *J. Chem. Phys.*, 1952, **20**, 837; C. J. Ballhausen and H. B. Gray, *Molecular Orbital Theory*, 1965, Benjamin, New York.